Draft version January 27, 2016
Preprint typeset using LaTeX style emulateapj v. 08/22/09

arXiv:1601.06836v1 [astro-ph.HE] 25 Jan 2016

IRON OPACITY BUMP CHANGES THE STABILITY AND STRUCTURE OF ACCRETION DISKS IN ACTIVE GALACTIC NUCLEI

Yan-Fei Jiang(姜燕飞)[1,4], Shane W. Davis[2] & James M. Stone[3]
[1]Harvard-Smithsonian Center for Astrophysics, 60 Garden Street, Cambridge, MA 02138, USA
[2]Department of Astronomy, University of Virginia, P.O. Box 400325, Charlottesville, VA 22904-4325, USA and
[3]Department of Astrophysical Sciences, Princeton University, Princeton, NJ 08544, USA

Draft version January 27, 2016

ABSTRACT

Accretion disks around supermassive black holes have regions where the Rosseland mean opacity can be much larger than the electron scattering opacity primarily due to the large number of bound-bound transitions in iron. We study the effects of this iron opacity "bump" on the thermal stability and vertical structure of radiation pressure dominated accretion disks, utilizing three dimensional radiation magneto-hydrodynamic simulations in the local shearing box approximation. The simulations self-consistently calculate the heating due to MHD turbulence caused by magneto-rotational instability and radiative cooling by using the radiative transfer module based on a variable Eddington tensor in Athena. For a 5×10^8 solar mass black hole with $\sim 3\%$ of the Eddington luminosity, a model including the iron opacity bump maintains its structure for more than 10 thermal times without showing significant signs of thermal runaway. In contrast, if only electron scattering and free-free opacity are included as in the standard thin disk model, the disk collapses on the thermal time scale. The difference is caused by a combination of 1) an anti-correlation between the total optical depth and the temperature, and 2) enhanced vertical advective energy transport. These results suggest that the iron opacity bump may have a strong impact on the stability and structure of AGN accretion disks, and may contribute to a dependence of AGN properties on metallicity. Since this opacity is relevant primarily in UV emitting regions of the flow, it may help to explain discrepancies between observation and theory that are unique to AGNs.

Subject headings: accretion disks − (magnetohydrodynamics:) MHD − methods: numerical − radiative transfer

1. INTRODUCTION

The radiation from active galactic nuclei (AGNs) is widely believed to be produced from the gas accreted by supermassive black holes through their accretion disks (e.g., Malkan 1983). The standard α disk model (Shakura & Sunyaev 1973) is commonly used to model the structures of accretion disks in most AGNs, mainly because the temperature predicted by the α disk model is roughly consistent with the big blue bump in AGN spectra (Elvis et al. 1994; Koratkar & Blaes 1999). However, there are discrepancies when detailed predictions of the α disk model are compared with AGN observations (see e.g. Koratkar & Blaes 1999).

From the theoretical point of view, the main puzzle is the outcome of the inflow ("viscous") and thermal instabilities in α disks that are radiation pressure dominated, which should be the case for the inner region of AGN disks (Lightman & Eardley 1974; Shakura & Sunyaev 1976). The thermal instability, which should grow faster than the inflow instability, exists because the cooling rate Q^- in this regime is proportional to the midplane pressure $P_{z,0}$ while the heating rate $Q^+ \propto P_{z,0}^2$ (Piran 1978). When the pressure is perturbed to be smaller (larger) than equilibrium value, Q^+ decreases (increases) faster compared with the change of Q^- and the disk will continue to cool down (heat up) and never return to the original equilibrium state. The existence of the radiation dominated thermal instability has been questioned (e.g. Stella & Rosner 1984; Merloni 2003). The first 3D local shearing box simulations with turbulence driven by the magneto-rotational instability (MRI, Balbus & Hawley 1991) and optically thick radiative cooling seemed consistent with thermal stability (Turner 2004; Hirose et al. 2009b), but more recent simulations performed in larger domains and using more sophisticated radiative transfer methods have found that the radiation dominated accretion disks still show signs of thermal runaway after a few thermal time scales (Jiang et al. 2013a). However, no clear evidence of rapid variability that might be consistent with the thermal instability has yet been observed in most AGNs. Although there has been speculations that recently discovered "change-look" AGNs (LaMassa et al. 2015; Ruan et al. 2015) may be caused by these instabilities, it is difficult to understand why the instabilities would uniquely manifest themselves only in this specific subset of AGNs.

Observationally, many properties of AGNs cannot be explained with the standard α disk model (Koratkar & Blaes 1999), in spite of the issue of thermal instability. The Spectrum Energy Distribution (SED) of most AGNs shows a turnover always around 1000 Å, almost independent of the black hole mass (Zheng et al. 1997; Bonning et al. 2007; Davis et al. 2007; Laor & Davis 2014, and references therein). The predicted Lyman edge is also not observed (Shull et al. 2012). The inferred size of the AGN accretion disks based on micro-lensing measurements (e.g. Morgan et al. 2010; Blackburne et al. 2011) or the lags between the variations in different continu-

[4] Einstein Fellow

ous bands (Edelson et al. 2015) is systematically larger than the half-light radius of the α disk model. A soft X-ray excess is also ubiquitously observed in bright AGNs (Crummy et al. 2006; Done et al. 2012; Done 2014), but is not easily explained by the α disk model if it results from continuum emission.

The order-of-magnitude temperature and density in the AGN accretion disks can actually be roughly estimated based on a few assumptions independent of any accretion disk model. If we assume the accreted gas is optically thick with typical Eddington luminosity $L_{\rm Edd} = 1.5 \times 10^{46} M_{\rm BH}/(10^8 M_\odot)$ erg/s, typical emission size to be the Schwarzschild radius $r_s = 3.0 \times 10^{13} M_{\rm BH}/(10^8 M_\odot)$ cm, then the effective temperature is $T \sim 3.9 \times 10^5 \left(M_{\rm BH}/10^8 M_\odot\right)^{-1/4}$ K. Density of the gas depends on the assumed inflow velocity, which is likely subsonic with respect to the radiation sound speed (Pringle 1981). As an order-of-magnitude estimate, we take it to be the gas isothermal sound speed with the effective temperature estimated above. With the typical mass accretion rate $\dot{M}_{\rm Edd} = 10 L_{Edd}/c^2 = 1.6 \times 10^{26} M_{\rm BH}/(10^8 M_\odot)$ g/s and inflow radius r_s, the typical density is $\rho \sim 2 \times 10^{-9}$ g/cm^3 for the $10^8 M_\odot$ black hole. The density and temperature in the α disk model are consistent with this simple estimate. However, this temperature and density regimes are very similar as in the envelope of massive stars (Paxton et al. 2011; Jiang et al. 2015). With non-negligible metallicity, the OPAL opacity project (Iglesias & Rogers 1996) shows that the Rosseland mean opacity can be significantly enhanced compared with the electron scattering value due to metals. In particular, the irons produce the well-known opacity bump around the temperature 1.8×10^5 K. The opacity drops rapidly with increasing or decreasing temperature and it only depends on the density weakly (Figure 2 of Jiang et al. 2015). As significant metals are indeed observed in the broad line regions of AGNs (Hamann & Ferland 1993; Dhanda et al. 2007), the iron opacity bump should exist in the AGN disks. However, the standard α disk model only includes the electron scattering and free-free opacities. Following Jiang et al. (2013a), we will calculate the turbulence from MRI without any α assumption and radiative transfer including the iron opacity bump self-consistently based on 3D radiation MHD simulations. Because optical depth is critical for the radiative cooling of the disk, we will study how the thermal stability and structures of the AGN disks will be affected by the iron opacity bump. Note that for accretion disks in X-ray binaries around stellar mass black holes, the disk midplane temperature in the inner region is too hot for iron opacity to play an important role, but it may play a role in the outer disk dynamics. Another example where opacity effects significantly change the dynamics of the disk is the hydrogen ionization instability in accretion disks around white dwarfs (Lasota 2001; Hirose et al. 2014).

This paper is organized as follows. We describe how we setup the simulations in § 2, and the initial and boundary conditions we use in § 3. Our primary results are described in § 4, while § 5 compares the simulation results with the α disk model and discusses the implications for AGN observations.

2. SIMULATION SETUP

We solve the same set of radiation MHD equations under the local shearing box approximation as equation (2) of Jiang et al. (2013a) given by. The simulation box is located at a fiducial radius $r_0 = 20$ Schwarzschild radii from a $M_{\rm BH} = 5 \times 10^8 M_\odot$ black hole. Keplerian rotation is assumed for the background flow with the orbital frequency $\Omega = 1.60 \times 10^{-6}$ s^{-1} and shear parameter $q = -d \ln \Omega / d \ln r = 3/2$. We solve these equations with the Godunov radiation MHD code as described and tested in Jiang et al. (2012) and Davis et al. (2012), with the improvements given by Jiang et al. (2013b). Under the shearing box approximation, heating is generated by the dissipation from MRI turbulence with the energy ultimately coming from work done by the shearing period boundary condition, while cooling is dominated by the photons leaving from the top and bottom of the simulation box.

For the opacities describing the interactions between the radiation and gas, we calculate the total Rosseland mean opacity κ_t based on the opacity table from the Modules for Experiments in Stellar Evolution (MESA, Paxton et al. 2011) for solar metallicity in order to capture the dependencies of the opacity on temperature and density correctly. This opacity table is originally from the OPAL opacity project (Iglesias & Rogers 1996) and has been successfully used to study the stability and structures of massive star envelopes (Jiang et al. 2015). The opacity as a function of temperature and density is shown in Figure 2 of Jiang et al. (2015), which also covers the relevant parameter space for AGN disks. The most important feature is the opacity bump caused by a large number of bound-bound transitions, most due to iron atoms, for temperatures around 1.8×10^5 K. This can be a factor of ~ 4 larger than the electron scattering opacity for solar metallicity. In order to split this Rosseland mean opacity into scattering and absorption terms (as only the absorption opacity enters the energy exchange terms in the radiation moment equations), we simply adopt the electron scattering opacity $\kappa_{\rm es} = 0.34$ cm^2 g^{-1} and subtract this from the Rosseland mean opacity. The Planck mean absorption opacity is taken to be the same as Rosseland mean absorption opacity for simplicity, although it is likely to be an underestimate since the Rosseland mean tends to more heavily weight frequencies with low opacity. For comparison, we also perform simulations with the "standard" thin disk model opacity, which only includes the electron scattering opacity $\kappa_{\rm es}$, Plank-mean free-free absorption opacity $\kappa_{\rm aP} = 3.7 \times 10^{53} \left(\rho^9/E_g^7\right)^{1/2}$ cm^2 g^{-1} and Rosseland-mean free-free absorption opacity $\kappa_{\rm aF} = 1.0 \times 10^{52} \left(\rho^9/E_g^7\right)^{1/2}$ cm^2 g^{-1}. Here $E_g = P_g/(\gamma - 1)$ is the gas internal energy with gas pressure P_g, density ρ and adiabatic index $\gamma = 5/3$. This combination of opacities has been used in most previous simulations, which focussed on hotter disks more appropriate to $\sim 10 M_\odot$ black hole X-ray binaries (Hirose et al. 2009b; Jiang et al. 2013a).

3. INITIAL AND BOUNDARY CONDITIONS

We construct the initial vertical profiles of the disk based on hydrostatic equilibrium and diffusion equation as in Hirose et al. (2009b) and Jiang et al. (2013a) but

with the the iron opacity bump included self-consistently. We assume the dissipation profile $dF_{r,z}/dz \propto \rho\kappa_t/\tau^{0.5}$, where τ is the optical depth from the nearest surface of the disk and $F_{r,z}$ is the vertical component of the radiation flux. If the total optical depth from the disk midplane to the surface is τ_0, by symmetry, the radiation flux as a function of τ within the photosphere is $F_{r,z} = F_{\max}\left(\tau_0^{0.5} - \tau^{0.5}\right)/\left(\tau_0^{0.5} - 1\right)$. Here we choose the initial maximum radiation flux $F_{\max} = 7.92 \times 10^{11}$ erg s^{-1} cm^{-2}, and $F_{r,z}$ is fixed to this value in the region where $\tau < 1$. We choose the midplane temperature 2.4×10^5 K and integrate vertically according to the diffusion equation $dE_r/d\tau = 3F_{r,z}/c$, where c is the speed of light. The total optical depth τ_0 is chosen such that at $\tau = 1$, $E_r = \sqrt{3}cF_{r,z}$. Initially, gas temperature T is set to be the same as the radiation temperature $T_r \equiv (E_r/a_r)^{0.25}$, where the radiation constant $a_r = 7.57\times10^{15}$ erg cm^{-3} K^{-4}. The initial density profile is constructed based on the equation of hydrostatic equilibrium $dP/dz = \kappa_t F_{r,z}/c - \Omega^2 z$ and $d\tau = -\rho\kappa_t dz$. The midplane density is adjusted to be 10^{-8} g cm^{-3} such that the initial total optical depth is $\tau_0 = 9.5 \times 10^5$. All the quantities above the photosphere are fixed to be the same values as at $\tau = 1$. Notice that in the initial condition, only the surface density Σ is the conserved quantity, while all the other quantities such as $\rho, T, \tau_0, F_{r,z}$ will adjust self-consistently during the simulation. The magnetic field is initialized in the same way as in Jiang et al. (2013a) with the initial ratio between gas pressure and magnetic pressure to be 12 at $z = 0$. The boundary conditions are also the same as in Jiang et al. (2013a). For the short characteristic module we use to calculate the variable Eddington tensor (VET), we use 80 angles per cell to capture the angular distribution of the radiation field. Sizes of the simulation box are all fixed to be $L_x = 0.87H_s$, $L_y = 3.48H_s$ and $L_z = 6.96H_s$, where H_s is the length unit listed in Table 1. The length unit is chosen based the total radiation flux $F_{\max}$ we get from the simulation (Table 1) as $H_s = \kappa_{\rm es}F_{\max}/(c\Omega^2)$. For the typical density ρ_0 and temperature T_0 given in table 1, it is related to the gas pressure scale height $H_g \equiv c_g/\Omega$ and radiation pressure scale height $H_r \equiv c_r/\Omega$ as $H_s = 8.57H_g = 2.25H_r$, where c_g is the isothermal sound speed for temperature T_0 and radiation sound speed $c_r = \sqrt{a_r T_0^4/(3\rho_0)}$. We use $64 \times 128 \times 512$ grids for x, y, z directions so that we have roughly 32 grids per radiation pressure scale height H_r. Following the convention in Athena (Stone et al. 2008), unit of the magnetic field is chosen so that magnetic permeability is one.

4. RESULTS

The initial evolutions of the disks are very similar for the cases with or without the iron opacity. The disk cools down slightly while MRI is still growing from the laminar initial condition during the first few orbits. However, once heating is generated by vigorous MHD turbulence from MRI, the disk undergoes quite different evolution histories for different opacities. We label the run with iron opacity bump as OPALR20, while three runs with just electron scattering and free-free opacities for comparison as ESR20a, ESR20b and ESR20c.

Table 1
Simulation Parameters of the run OPALR20

Ω / s^{-1}	1.60×10^{-6}
r_0 / cm	2.97×10^{15}
ρ_0/ g cm^{-3}	1.00×10^{-8}
T_0 / K	2.00×10^5
P_0 / dyn cm^{-2}	2.77×10^5
H_s / cm	2.81×10^{13}
Σ / g cm^{-2}	4.34×10^5
τ_0	2.31×10^5
$F_{\max}$/erg s^{-1} cm^{-2}	6.36×10^{12}

Note: The parameters Ω, r_0 and Σ are fixed for the simulation, while τ_0 and $F_{\max}$ are time averaged properties between 60 and 125 orbits. The density ρ_0, pressure P_0, temperature T_0 and scale height H_s are the fiducial units we use to describe the simulation. They are pretty close to the midplane density, temperature and characteristic disk scale height.

4.1. *Simulation History*

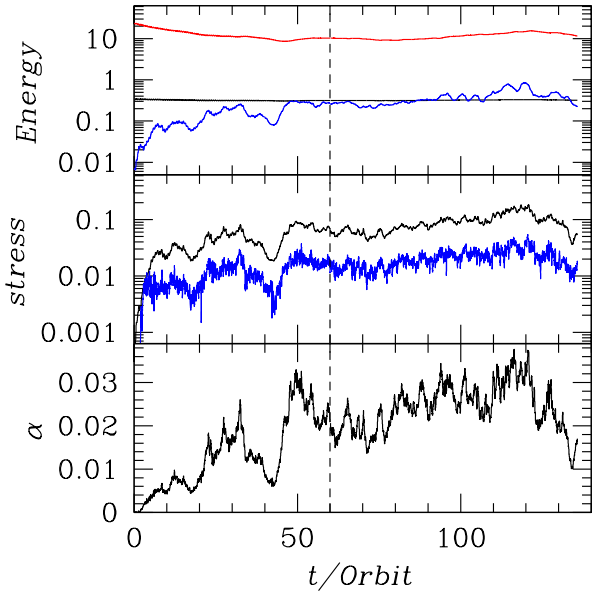

Figure 1. Top: histories of the volume averaged radiation energy density E_r (red line), gas internal energy E_g (black line) and magnetic energy density E_B (blue line) for the run OPALR20 with iron opacity bump. Middle: history of the volume averaged Maxwell stress $-B_xB_y$ (black line) and Reynolds stress $\rho v_x \delta v_y$ (blue line). Bottom: history of the α parameter, which is the ratio between the sum of the total Maxwell and Reynolds stress and the sum of the total radiation, gas and magnetic pressure. The vertical dashed line separates the first 60 orbits when Eddington approximation is adopted and the time with VET turned on. Units for the energy density and stress are P_0 as given in Table 1.

4.1.1. *The Run* OPALR20 *with Iron Opacity Bump*

For OPALR20, we first ran the simulation by setting the Eddington tensor $\mathsf{f} = 1/3\mathsf{I}$ and disk lasted for 60 orbits. Then the simulation is restarted with the short characteristic module turned on to calculate the VET self-consistently for another 75 orbits. Histories of the volume averaged energy densities for the whole simulation duration are shown in the top panel of Figure 1. Although we have run the simulation for more than 10 thermal time scales and E_r is more than 60 times larger

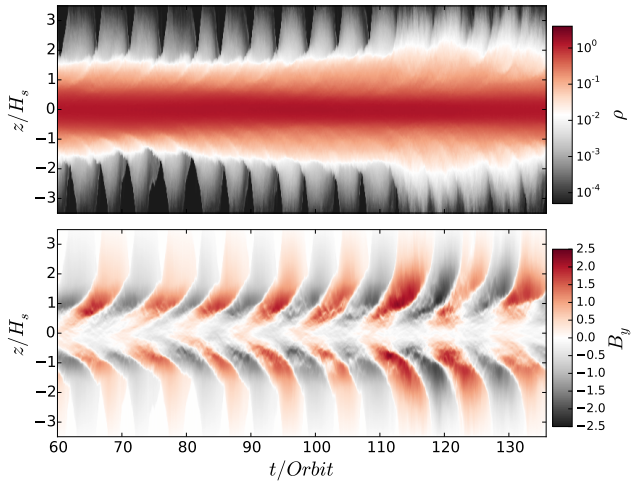

Figure 2. Space-time diagram of the density ρ (top panel, in unit of ρ_0) and azimuthal magnetic field B_y (bottom panel, in unit of $\sqrt{2P_0}$) for the run OPALR20.

than E_g, the radiation energy density E_r, gas internal energy E_g and magnetic energy density E_b do not show any thermal runaway behavior as shown in Jiang et al. (2013a). The radiation energy density E_r varies only by a factor of 2 while E_g is almost a constant. Magnetic energy density E_b shows a larger variation amplitude and it can change by a factor of 5 after the initial 60 orbits. Histories of the volume averaged Maxwell stress and Reynolds stress are shown in the middle panel of Figure 1, while history of the equivalent α parameter is shown in the bottom panel of Figure 1. Here α is calculated as the ratio between the time and volume averaged stress and total pressure, which is 0.025 after the first 60 orbits. The average ratio between the total Maxwell stress and Reynolds stress from the MRI turbulence is 4.33 while the average ratio between the total Maxwell stress and magnetic pressure is 0.25. These statistical properties are consistent with previous local shearing box or global simulations of MRI turbulence, either with isothermal equation of state or self-consistent radiative transfer (Turner et al. 2003; Guan et al. 2009; Hawley et al. 2011; Sorathia et al. 2012; Jiang et al. 2013b).

The space-time diagram of the density ρ and toroidal magnetic field B_y for this simulation after the first 60 orbits are shown in Figure 2, where the well-known butterfly diagram is clearly observed. The turbulent magnetic field generated by MRI peaks around $z \approx \pm H_s$. The butterfly pattern can be attributed to regions of strong B_y buoyantly rising away from the midplane. This pattern of B_y reverses roughly every 10 orbits. The buoyantly rising magnetic field provides enhanced pressure support and causes the density scale height near the surface to rise and fall following the same pattern. These buoyant motions also affect the energy transport inside the disk, and are discuss further in section 4.2.

To confirm that the disk is in roughly thermal equilibrium, we compare the total heating Q^+ and cooling Q^- rates according to equations (2) and (3) in Jiang et al. (2013a), which are shown in the top panel of Figure 3. Indeed, Q^+ and Q^- track each other very well and midplane pressure only varies in a very small dynamic range. This is quite different from Figure 2 of Jiang et al. (2013a), where $Q+$ and Q^- diverge from each other when the disk undergoes thermal runaway. Because the disk is in thermal equilibrium, we also cannot measure the dependence of Q^+ and Q^- on $P_{z,0}$ as we did in Jiang et al. (2013a).

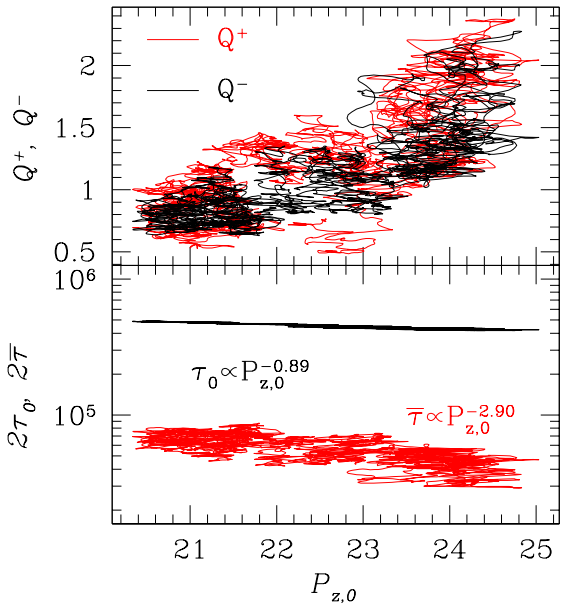

Figure 3. Top: change of the heating Q^+ and cooling Q^- rates per unit area as a function of the midplane total pressure $P_{z,0}$ for the run OPALR20. Bottom: change of the total optical depth τ_0 and flux weighted optical depth $\bar{\tau}$ as a function of $P_{z,0}$. The midplane pressure is in unit of P_0 while the units for Q^+ and Q^- are $P_0 H_s \Omega$.

4.1.2. *Three Runs Without the Iron Opacity Bump*

To confirm that the different behaviors we see between the run OPALR20 and the simulations shown in Jiang et al. (2013a) are indeed caused by the iron opacity bump, we have done three comparison runs by only including the electron scattering and free-free opacities as in Jiang et al. (2013a). For the run ESR20a, we use the same surface density as in OPALR20. Because electron scattering opacity is smaller than the iron opacity, the total optical depth τ_0 is only 34% of the value in OPALR20. For the run ESR20b, we increase the surface density by a factor of 2 so that the total optical depth is closer to the value in OPALR20. We do not increase the surface density to match the τ_0 in OPALR20, because then the surface density is larger than the maximum surface density allowed by the thin disk model with $\alpha = 0.02 - 0.03$. Initial conditions for the two runs are constructed in the same way as described in Section 3. To test the effect of the initial condition, for the run ESR20c, we restart the simulation OPALR20 at 60 orbit by changing the opacity to be electron scattering and free-free opacities while keeping all the other quantities unchanged. In this way, ESR20c has exactly the same turbulence as OPALR20 to start with. All the other parameters of the three runs, such as box size and resolution, are the same as the run OPALR20.

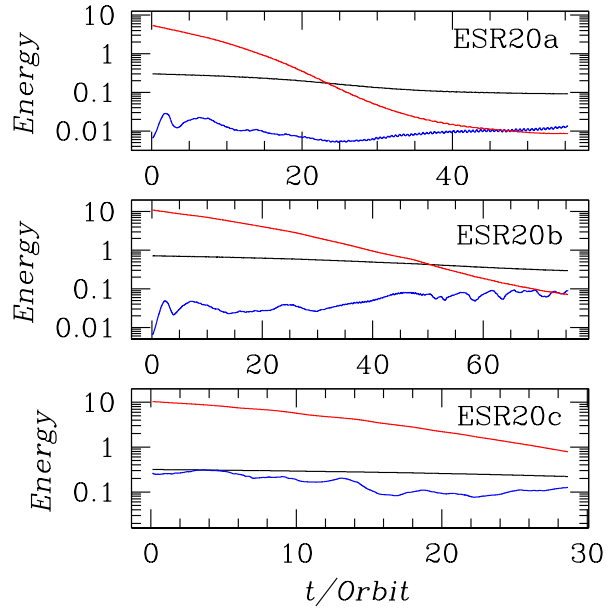

Figure 4. Histories of the volume averaged energy densities E_r (red lines), E_g (black lines) and E_B (blue lines). From the top to bottom, they are for the three runs ESR20a, ESR20b and ESR20c, which only include the electron scattering and free-free opacities. Units of the energy densities are P_0.

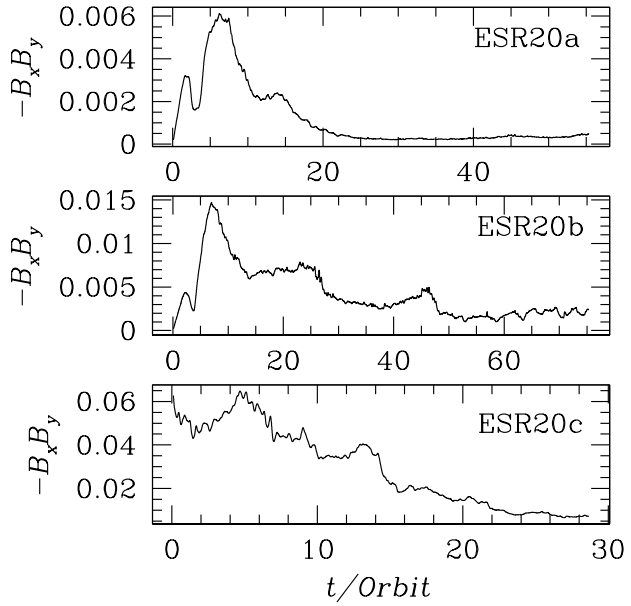

Figure 5. Histories of the volume averaged Maxwell stress for the three runs ESR20a, ESR20b and ESR20c. Units of the stress are P_0.

Histories of the volume averaged energy densities and Maxwell stress of the three runs are shown in Figure 4 and 5. For all the three cases, the disks continue to cool down and collapse within $\sim 4-6$ thermal time scales. For ESR20a and ESR20b where we start the simulations from the laminar state, they collapse more quickly because there is no heating at the beginning. The Maxwell stress reaches the peak within the initial ~ 6 orbits and

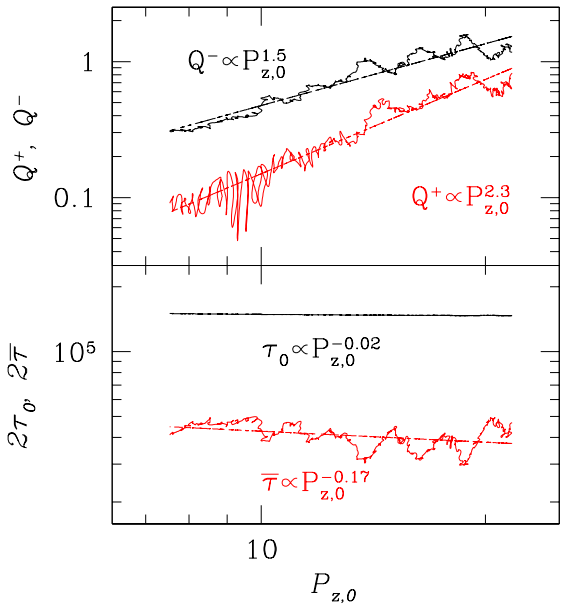

Figure 6. Change of the heating Q^+, cooling Q^- rates per unit area (top) and total optical depth τ_0 as well as flux weighted optical depth $\bar{\tau}$ (bottom) as a function of the midplane total pressure $P_{z,0}$ for the run ESR20c. The units are the same as in Figure 3.

declines while the disks collapse. They do not reach any radiation pressure dominated thermal equilibrium state as the run OPALR20. Instead, they behave in a very similar way as the simulation RSVET shown in Jiang et al. (2013a). For the run ESR20c where heating from the MRI turbulence exists from the beginning, the initial radiation energy density of the disk is pretty close to value as predicted by the radiation pressure dominated standard thin disk solution with the same surface density and an equivalent $\alpha = 0.02$. However, with only electron scattering and free-free opacities, the disk does not adjust itself to reach a radiation pressure dominated equilibrium state. Instead, E_r drops by one order of magnitude continuously within 30 orbits. The Maxwell stress also decreases while the disk collapses. The dependences of heating Q^+ and cooling Q^- rate on the midplane pressure for the run ESR20c are shown in the top panel of Figure 6, which are very similar to the simulation RMLVET reported by Jiang et al. (2013a). The heating rate does have a stronger sensitivity to the midplane pressure compared with the cooling rate when the thermal runaway happens. Compared with OPALR20, the three runs confirm that the different behaviors are indeed caused by the iron opacity bump, as the opacity law is the only difference between them.

4.2. *Vertical Structure of the Disk in the Run* OPALR20

In order to investigate the reasons why the iron opacity bump can make the radiation pressure dominated disks last much longer, we first study the time averaged vertical structures of disk in the run OPALR20. We compute time averages starting at 60 orbits so that only the VET portion of the runs is included.

The horizontally averaged vertical profiles of ρ, T_g, T_r and κ_t are shown in Figure 7. The midplane temperature is larger than T_0 so that the peak of the Fe opacity bump

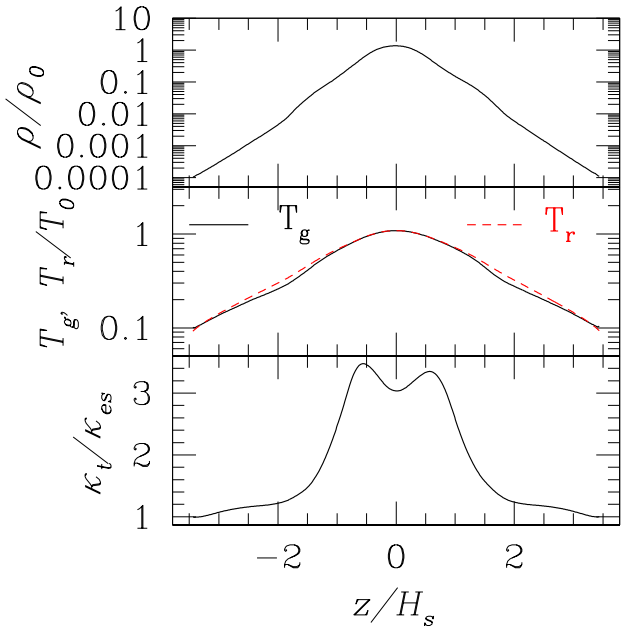

Figure 7. Time and horizontally averaged vertical profiles of density ρ (top panel), gas (T_g) and radiation (T_r) temperature (middle panel), as well as the Rosseland mean opacity κ_t (bottom panel) for the run OPALR20.

occurs off the midplane. The opacity κ_t peaks around $\approx 0.5H_s$ and drops both when the temperature decreases towards the photosphere and when it increases towards the midplane. At the peak, κ_t is more than three times the value of the electron scattering opacity for the solar metallicity we adopt. The iron opacity has a very weak dependence on density (Figure 2 of Jiang et al. 2015). The rapid drop around $\pm H_s$ is primarily because of the drop in temperature.

Because local dynamic time scale $1/\Omega$ is much shorter than the thermal time scale, we expect the hydrostatic equilibrium to be maintained very well. This means the time averaged vertical accelerations due to various forces should be roughly balanced as

$$a_g = a_r + a_{gas} + a_B, \tag{1}$$

where $a_g = \Omega^2 z$ is the vertical component of the gravitational acceleration due to the central black hole. The accelerations due to radiation (a_r), gas (a_{gas}) and magnetic field (a_B) are calculated as

$$\begin{aligned} a_r &= \frac{\kappa_t F_{r,z0}}{c}, \\ a_{gas} &= -\frac{\partial P_g}{\rho \partial z}, \\ a_B &= -\frac{1}{2\rho}\frac{\partial}{\partial z}\left(B_x^2 + B_y^2\right) \\ &\quad + \frac{1}{\rho}\left(B_x\frac{\partial B_z}{\partial x} + B_y\frac{\partial B_z}{\partial y}\right). \end{aligned} \tag{2}$$

Here B_x and B_z are the radial and vertical components of the magnetic field and a_B includes both the accelerations due to magnetic pressure gradient and vertical component of magnetic tension (Blaes et al. 2011). Notice that only the diffusive radiation flux $F_{r,z0}$ contributes to the radiation acceleration a_r. The time averaged vertical profiles of these accelerations are shown in the top panel of Figure 8, which shows that equation (1) is indeed satisfied very well. The vertical profiles of radiation pressure P_r, gas pressure P_g and magnetic pressure P_b are shown in the bottom panel of Figure 8. Near the disk midplane when $|z| \lesssim 1.8H_s$, the disk is radiation pressure dominated, which is also consistent with the fact a_r is much larger than a_{gas} and a_B in this region. Beyond that, magnetic pressure becomes dominant. The magnetic pressure first increases with distance near the disk midplane and peaks around $\pm 0.7H_s$. Then it drops with height. This feature is commonly observed in previous MRI simulations (e.g., Miller & Stone 2000; Hirose et al. 2006; Blaes et al. 2011; Jiang et al. 2014b). The ratio between radiation pressure and gas pressure varies from ~ 15 to more than 100.

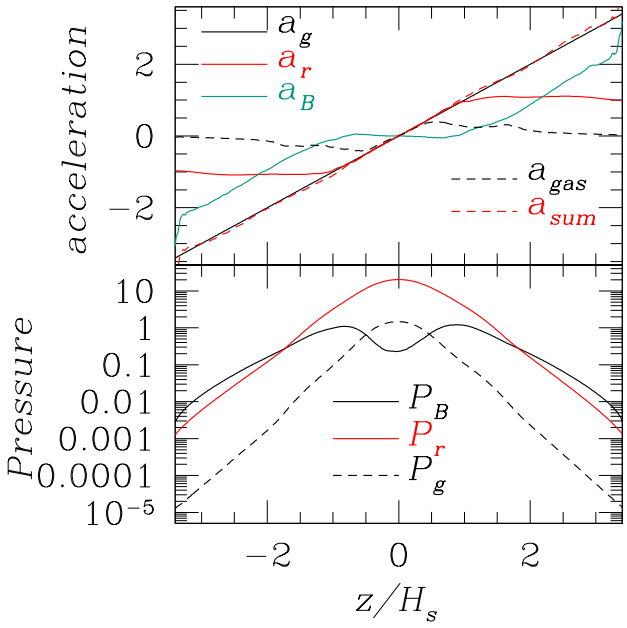

Figure 8. Top: time and horizontally averaged vertical profiles of accelerations due to gas a_{gas}, radiation a_r and magnetic field a_B for the run OPALR20. The sum of the three accelerations is a_{sum} while a_g is the vertical component of the gravitational acceleration due to the central black hole. Bottom: averaged vertical profiles of gas pressure P_g, radiation pressure P_r and magnetic pressure P_B. Units for the accelerations are $\Omega^2 H_s$ while the pressure units are P_0.

4.2.1. *Change of the Optical Depth with Temperature*

Because of the sensitive dependence of the iron opacity bump with temperature, it will only enhance the opacity significantly within a narrow temperature range, which corresponds to a certain vertical range of the disk. The contribution of the iron opacity bump to the total optical depth is dominated by $\tau_p = \rho_p \kappa_p H_p$, where ρ_p and κ_p are the density and opacity at the opacity peak while H_p is proportional to the disk scale height. For a constant surface density, this can be rewritten as $\tau_p = \rho_p \kappa_p \Sigma / \rho_{z,0}$, where $\rho_{z,0}$ is the density at disk midplane. When the disk becomes hotter and midplane temperature increases, the iron opacity peak will move to larger height and thus

$\rho_p/\rho_{z,0}$ decrease. When the disk becomes colder and midplane temperature drops, the iron opacity peak will move towards the midplane and $\rho_p/\rho_{z,0}$ increases. Because κ_p only depends on density weakly, as long as the whole iron opacity bump is included in the disk and it is the dominant opacity, this means the total optical depth will decrease when the disk becomes hotter, and increase with the disk becomes colder.

To confirm this, we plot the total optical depth $2\tau_0$ as a function of the midplane pressure (dominated by P_r) for the run OPALR20 after the initial 60 orbits at the bottom panel of Figure 3, which shows a very clear anti-correlation between τ_0 and $P_{z,0}$. A simple power law fitting shows that $\tau_0 \propto P_{z,0}^{-0.89}$ in this simulation. This is completely different from the electron scattering dominated case as shown in the bottom panel of Figure 6 for the run ESR20c, where τ_0 is almost independent of $P_{z,0}$ as expected. This is critical for the thermal instability, because in the standard thin disk model, the cooling rate $Q^- \propto P_{z,0}/\tau_0$. With this close to linear anti-correlation between τ_0 and $P_{z,0}$, the sensitivity of the cooling rate to midplane pressure is enhanced. This is one important reason why the thermal instability is suppressed and the disk can last much longer.

One crude way to understand the anti-correlation between τ_0 and $P_{z,0}$ quantitively is by assuming a constant ratio between radiation pressure and gas pressure. This is expected with efficient convection in the radiation pressure dominated regime so that the radiation entropy per unit mass, which is proportional to P_r/P_g, is roughly a constant. This is clearly not the case for the whole disk as this ratio increases from ~ 15 near the disk midplane to more than 100 near the surface. However, in the region when $|z| \lesssim 0.5H_s$, P_r/P_g does not vary too much and this is not a very bad assumption. Once we adopt this assumption, we have $\rho_p/\rho_{z,0} = (T_p/T_{z,0})^3$, where $T_{z,0}$ is the midplane temperature. Because the iron opacity peak only exists for a roughly fixed temperature T_p and $P_{z,0} \propto T_{z,0}^4$ in the radiation pressure dominated regime, the total optical depth contributed by the iron opacity peak can be roughly estimated as $\tau_p \propto P_{z,0}^{-0.75}$, which is actually pretty close to what we get from the simulation.

4.2.2. *Vertical Energy Transport*

As shown in the top panel of Figure 3, during the thermal equilibrium state, the total heating rate Q^+ is balanced by the total cooling rate Q^-, where Q^- is dominated by radiative cooling. In the standard thin disk model, only the diffusive radiation flux is considered for the vertical radiative cooling everywhere. This is not necessary the case as photons can also be advected out with the buoyantly rising fluid elements (Blaes et al. 2011; Jiang et al. 2014a). The total energy flux carried by the photons is the lab frame radiation flux $F_{r,z}$, which is the sum of the diffusive radiation flux $F_{r,z0}$ and radiation enthalpy flux

$$F_{r,z} = F_{r,z0} + v_z E_r + \boldsymbol{v} \cdot \mathsf{P_r}|_z \,. \tag{3}$$

Here $\boldsymbol{v}$ is the fluid velocity and $\mathsf{P_r}$ is the radiation pressure tensor. The net advection flux is

$$F_{adv} = v_z E_r. \tag{4}$$

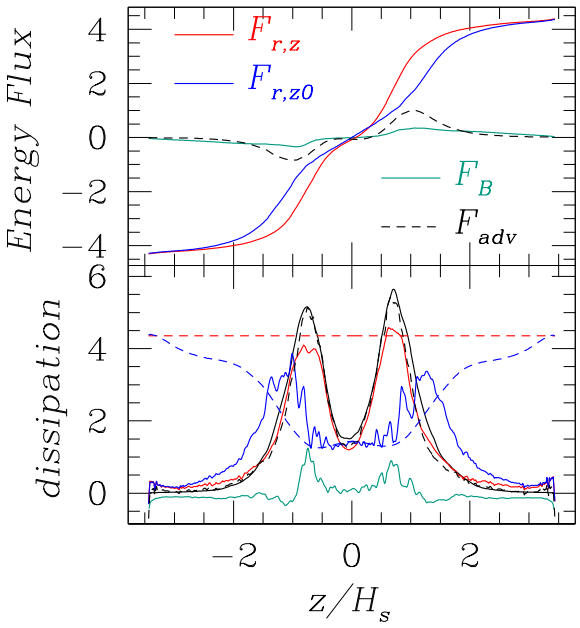

Figure 9. Top: time and horizontally averaged vertical profiles of lab frame radiation flux $F_{r,z}$, diffusive radiation flux $F_{r,z0}$, advective radiation flux F_{adv} and Poynting flux F_B. Bottom: averaged vertical profiles of local dissipation rate. The solid black line is the work done by the stress at each height $q\Omega(-B_xB_y + \rho v_x \delta v_y)$. The solid red, blue and green lines are $dF_{r,z}/dz$, $dF_{r,z0}/dz$ and dF_B/dz, respectively. The dashed black line is the sum of $dF_{r,z}/dz$ and dF_B/dz. The dashed red line is the critical dissipation rate $c\Omega^2/\kappa_{\rm es}$, while the dashed blue line is $c\Omega^2/\kappa_t$. Units for the energy flux and dissipation are $c_g P_0$ and $c_g P_0/H_s$.

Another important component of energy flux is the Poynting flux

$$F_B = B^2 v_z - (\boldsymbol{B} \cdot \boldsymbol{v})\, B_z. \tag{5}$$

The mechanical energy flux and gas enthalpy flux are small and we will not show them here. Time averaged vertical profiles of these energy fluxes are shown in the top panel of Figure 9. The local dissipation rates at each height are simply $q_r^- = dF_{r,z}/dz$, $dF_{r,z0}/dz$, dF_{adv}/dz and $q_B^- = dF_B/dz$. The work done by the stress at each height is $q^+ = q\Omega\,(-B_xB_y + \rho v_x \delta v_y)$. These local heating and cooling rates are shown in the bottom panel of Figure 9. In the thermal equilibrium state, local energy conservation requires

$$q^+ = q_r^- + q_B^-. \tag{6}$$

Time averaged vertical profiles of the left and right hand sides are shown as the solid and dashed black lines in the bottom panel of Figure 9, which shows that they do agree very well.

Around $z = \pm H_s$, there is a big difference between $F_{r,z}$ and $F_{r,z0}$, because there is a significant advection flux F_{adv}, which is comparable to $F_{r,z0}$. The nature of the advection flux will be discussed in the next section. The importance of the advection flux was first pointed out by Hirose et al. (2009b) and further explored in later work (Blaes et al. 2011; Jiang et al. 2013a). Significant advective transport is also observed in the global radiation MHD simulation of super-Eddington accretion disk by Jiang et al. (2014a). The advection flux drops around $\pm 2H_s$ as energy is increasingly transported by the dif-

fusive flux. Because the advection flux transports energy from the region near the midplane of the disk to the part closer to the surface in spite of the large optical depth, only the dissipation rate $dF_{r,z}/dz$ follows the heating rate q^+ and the vertical distribution of $dF_{r,z0}/dz$ is much broader. The peak of the heating rate q^+ is offset from the midplane and consistent with the peak of the magnetic pressure P_B shown in the bottom panel of Figure 8. The Poynting flux also peaks at the same location as q^+ and drops quickly with height.

4.2.3. *Nature of the Advection Flux*

The advection flux plays an important role for the stability and structure of the disk. Particularly with the iron opacity bump, it is significantly enhanced with respect to the electron scattering case for the reasons we will explain now. The advection flux is associated with the buoyantly rising pattern of the butterfly diagram shown in Figure 2. Around $z = \pm H_s$, the local optical depth per typical scale height H_s is $\tau = \rho\kappa_t H_s = 3.77\times10^4$, which is larger than the critical optical depth $\tau_c \equiv c/c_g = 5.69\times10^3$ defined in Jiang et al. (2015). According to the criterion of efficient radiation pressure dominated convection studied by Jiang et al. (2015), the photon diffusion time scale is much longer than any local dynamic time scale when $\tau > \tau_c$ so that photons can be trapped and advected with the buoyantly rising fluid elements. Around $\pm2H_s$, the local optical depth τ drops to 7.61×10^2, which is much smaller than τ_c. The diffusion time becomes short and the photons cannot be trapped anymore. The photons are released and transported out by the diffusive flux. The fluid elements must eventually fall back (on average) since we do not observe a net outward mass flux when average over dynamo cycles. However, the falling fluid elements are (on average) colder compared with rising elements because radiative energy is lost due to photon diffusion near the surface. Thus, there is a net vertical advective energy flux. Since the advection flux is much less sensitive to the optical depth, the net radiation flux at the surface of the disk can becomes much larger for a given $P_{z,0}$ than the value $\sim cP_{z,0}/\tau_0$ predicted by the diffusion equation.

Blaes et al. (2011) provide a detailed study on why the fluid elements rise buoyantly. Buoyant motion is *not* driven by the standard convective instability because the entropy profile is stable even when radiation entropy is included. Instead, it is the nonlinear outcome of the anti-correlation between density and magnetic field fluctuations in the MRI turbulence. In the radiation pressure dominated regime, large density and magnetic field fluctuations can be produced by MRI turbulence (Turner et al. 2003; Jiang et al. 2013b). If we consider horizontal variations at fixed height, low density regions have larger magnetic pressure to maintain the pressure balance horizontally. Therefore, low density, highly magnetized regions rise buoyantly (and vice versa). We have confirmed the presence of this effect in the run OPALR20. Figure 10 shows the horizontal slice at $z = H_s$ of density, magnetic pressure, radiation pressure and Maxwell stress at 100 orbit. The relatively lower density regions have stronger magnetic pressure, and also relatively lower radiation pressure to maintain the horizontal pressure balance. The Maxwell stress is well correlated with the magnetic pressure. The fluctuations can be quantified by the standard deviations, while the anti-correlation between density and magnetic pressure can be quantified by the cross correlation coefficient

$$\sigma_{\rho,B^2} = \frac{\langle(\rho-\overline{\rho})\left(B^2-\overline{B^2}\right)\rangle}{\sigma_\rho\sigma_{B^2}}, \tag{7}$$

where $\langle\cdot\rangle$ means horizontal average of the quantity and $\overline{\rho}$ and $\overline{B^2}$ are the horizontally averaged ρ and B^2 at each height. The standard deviations of ρ and B^2 are σ_ρ and σ_{B^2}. The top panel of Figure 11 shows the vertical profiles of the standard deviations of ρ and $P_t \equiv P_B+P_r+P_g$ scaled with the horizontally averaged ρ and P_t. The time averaged vertical profile of σ_{ρ,B^2} is shown at the bottom panel of Figure 11. It is clear that density fluctuations are much larger than the fluctuations of total pressure. The relative fluctuation σ_ρ/ρ can reach 30% at $\pm H_s$. There is a strong anti-correlation between density and magnetic pressure fluctuations as σ_{ρ,B^2} is negative for $|z| \lesssim 1.5H_s$.

The total flux $F_{\rm max}$ we get from the simulation only corresponds to $\sim 2\%-3\%$ Eddington accretion rate defined based on the electron scattering opacity. But we already observe significant advection flux in this simulation with iron opacity. For the comparison runs ESR20a, ESR20b and ESR20c, advection flux is negligible everywhere. For the electron scattering dominated simulations presented in Jiang et al. (2013a), the advection flux only became comparable to the local diffusive flux when the total radiation flux was more than 10% Eddington luminosity. Therefore, it seems that we are seeing an enhancement of the advection flux in the simulation with the additional Fe opacity.

One reason for the enhanced advective flux is that the higher opacity requires it. The amount of energy that can be transported by the diffusive flux is actually constrained by the hydrostatic equilibrium, because in the radiation pressure dominated regime $F_{r,z0} = c\Omega^2 z/\kappa_t$ and $dF_{r,z0}/dz = c\Omega^2/\kappa_t$. However, the local heating rate from the MRI turbulence q^+ is not limited by the opacity. As shown in the bottom panel of Figure 9, q^+ is much larger than $dF_{r,z0}/dz$. In order to maintain a thermal equilibrium state, the excess energy must be carried out by advection. Notice that $dF_{r,z0}/dz$ is significantly below the red dashed curved corresponding to $c\Omega^2/\kappa_{\rm es}$ in Figure 9 because $\kappa_t > \kappa_{\rm es}$. Comparison with Figure 2 of Blaes et al. (2011) shows that $dF_{r,z0}/dz$ must instead follow the $c\Omega^2/\kappa_{\rm es}$ curve in electron scattering dominated simulations, at least for the inner few scale heights. Since $dF_{r,z0}/dz$, and therefore $F_{r,z0}$, must be higher in this electron scattering dominated case, there is less need for advective flux to transport energy.

It also seems to be the case that the simulations with Fe opacity are less stable to magnetic buoyancy instabilities. We can considier this by comparing the hydrodynamic and magnetohydrodynamic Brunt-Väisälä frequencies as done by Blaes et al. (2011). Following equations (27), (28) and (29) in Blaes et al. (2011), the square of the hydrodynamic Brunt-Väisälä frequency is

$$N^2 = a_g\left(\frac{1}{\Gamma_1}\frac{d\ln\left(P_r+P_g\right)}{dz} - \frac{d\ln\rho}{dz}\right), \tag{8}$$

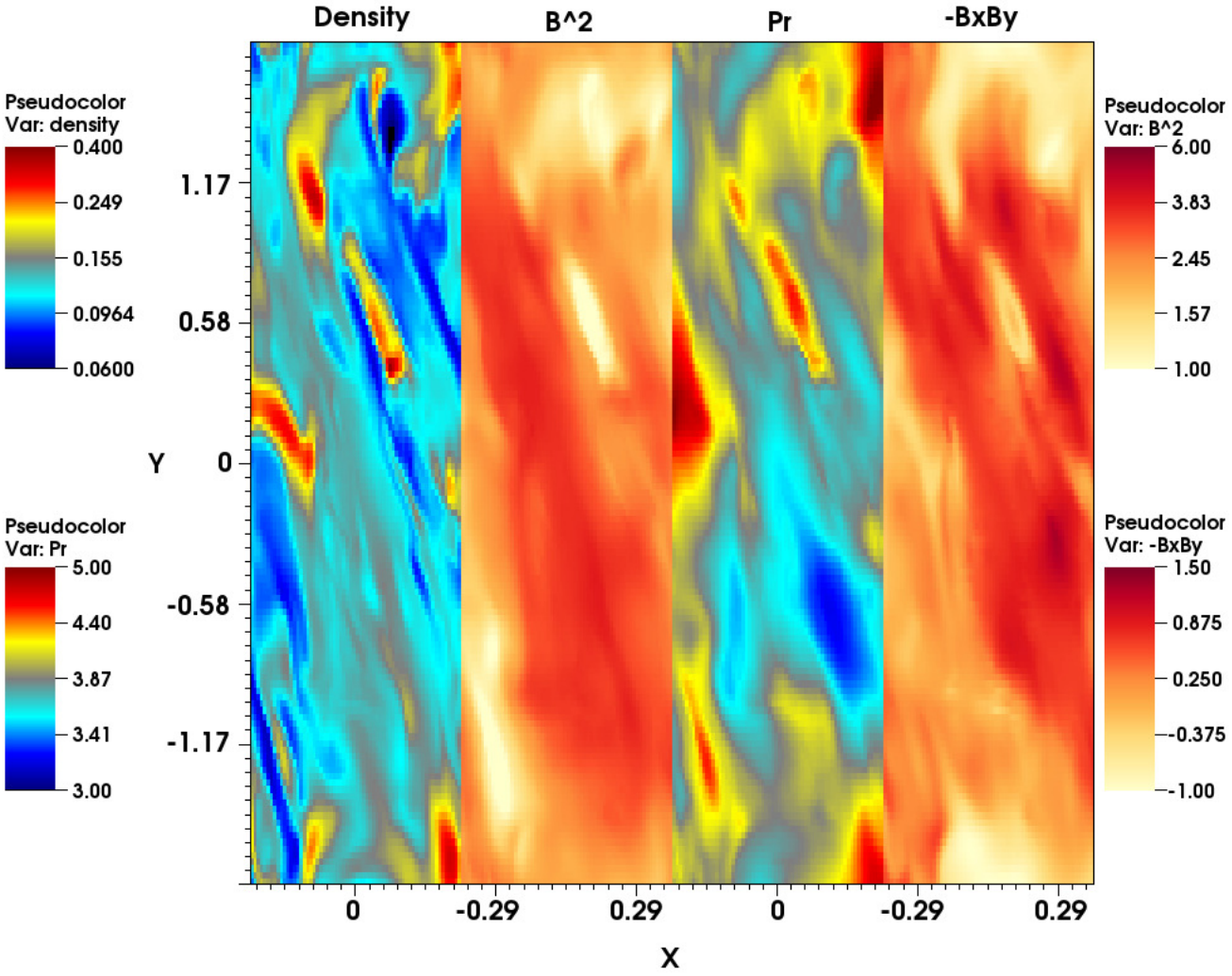

Figure 10. Horizontal slice of density, magnetic pressure, radiation pressure and Maxwell stress at $z = H_s$ for the run OPALR20 at 100 orbit.

where Γ_1 is the first adiabatic index defined in equation (15) of Jiang et al. (2015). Negative N^2 will indicate that it is unstable to convection. In the regime when the diffusion time scale is longer than the local dynamic time scale, the magnetic Brunt-Väisälä frequency can be defined as

$$N^2_{\rm mag} = N^2 + \frac{a_g v_A^2}{c_t^2}\frac{d\ln B}{dz}, \tag{9}$$

where v_A is the Alfvén velocity and $c_t^2 \equiv \Gamma_1 (P_r + P_g)/\rho$. When the diffusion time scale is much shorter than the local dynamic time scale so that diffusion is rapid, the relevant magnetic Brunt-Väisälä frequency is

$$N^2_{\rm mag,r} = \frac{a_g v_A^2}{c_t^2 + v_A^2}\frac{d\ln B}{dz}. \tag{10}$$

Undulatory Parker instability will happen when $N^2_{\rm mag}$ or $N^2_{\rm mag,r}$ become negative in the appropriate regime. Time averaged vertical profiles of N^2, $N^2_{\rm mag}$ and $N^2_{\rm mag,r}$ are shown in Figure 12. Here we first calculate the Brunt-Väisälä frequencies based on the horizontally averaged vertical profiles at each snapshot and then time average them. Figure 12 shows the averaged vertical profiles of N^2, $N^2_{\rm mag}$ and $N^2_{\rm mag,r}$. Consistent with Blaes et al. (2011), N^2 is positive so that the disk is stable to hydrodynamic convection. However, N^2 first increases with height within $\pm 0.7 H_s$ and then drops and reaches a minimum $\sim 0.03\Omega^2$ around $\pm 1.2 - 1.5 H_s$. This minimum does not exist in the electron scattering case shown in Blaes et al. (2011) and it is caused by the iron opacity peak around $\pm 0.7 H_s$ (see the bottom panel of Figure 7).

Because magnetic pressure also peaks near $\pm 0.7 H_s$ and decreases with height after the peak, it makes the magnetic Brunt-Väisälä frequency $N^2_{\rm mag}$ to become negative around $\pm H_s$ as shown in Figure 12, although magnetic pressure is still much smaller than the radiation pressure there. This means the region that is unstable to Parker instability is much deeper compared with the electron scattering opacity dominated case. Above $\pm 1.5 H_s$, diffusion is rapid and the relevant magnetic Brunt-Väisälä frequency is $N^2_{\rm mag,r}$, which is also negative. This mag-

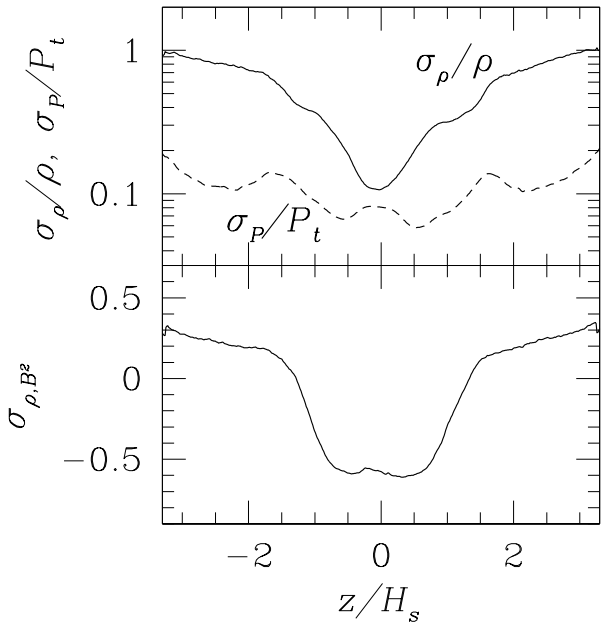

Figure 11. Top: time averaged vertical profiles of the standard deviations of density ρ and total pressure P_t scaled with the horizontally averaged values for the run OPALR20. Bottom: time averaged vertical profile of the cross correlation between ρ and B^2.

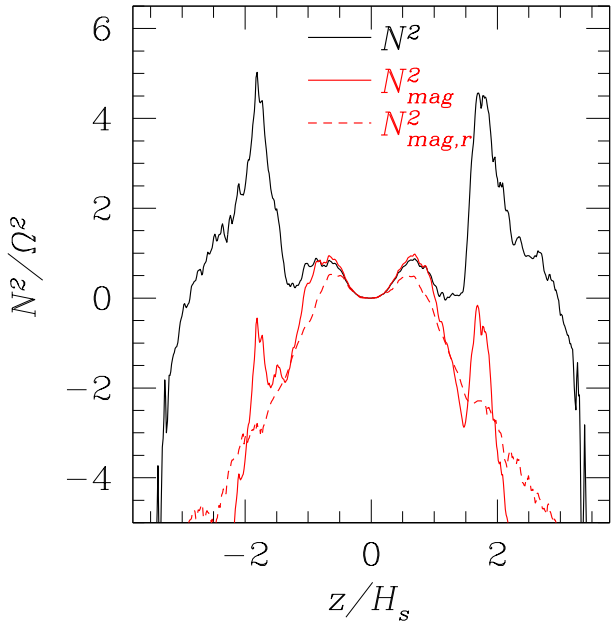

Figure 12. Time averaged vertical profiles of the hydrodynamic and magnetohydrodynamic Brunt-Väisälä frequencies N^2, $N^2_{\rm mag}$ and $N^2_{\rm mag,r}$ for the run OPALR20.

netic pressure dominated region is Parker unstable, as pointed out by Blaes et al. (2011). Because photons and gas are tightly coupled around $\pm H_s$ ($\tau > \tau_c$), the Parker instability enhances the buoyancy and theadvection flux as shown in Figure 9. Above $\pm 1.5H_s$ because of rapid diffusion, even though N^2 and $N^2_{\rm mag,r}$ are negative, they do not cause any significant advection flux as in the inefficient convection case studied by Jiang et al. (2015).

5. DISCUSSIONS AND CONCLUSIONS

By including the iron opacity bump in 3D local shearing box radiation MHD simulation of AGN disks, we show that the radiation pressure dominated accretion disks can survive many thermal time scales without showing significant thermal runaways. In contrast, if we just change the opacity to be electron scattering plus free-free as in the standard α disk model, the disk collapses quickly. The iron opacity bump can make the radiation pressure dominated accretion disks more stable because it causes the total optical depth to anti-correlate with the midplane pressure, and it enhances the advective cooling. Both effects increases the cooling rate and make the cooling rate change as fast as the heating rate. These results have a wide range of implications for AGN observations.

5.1. *Comparisons with the α disk model*

Neither of two effects we have identified are included in the standard thin disk model. Although we only have solutions for one set of parameters here, we expect the advection flux will also increase with increasing total pressure, because the amount of energy that can be transported by the diffusive flux is limited by the hydrostatic equilibrium. The excess heating will be transported by the advection flux to maintain thermal equilibrium.

Steady state vertical structure of a radiation pressure dominated disk is constrained by the equations of hydrostatic equilibrium

$$\frac{dP_r}{dz} = -\rho\Omega^2 z, \tag{11}$$

and thermal equilibrium

$$\alpha P_{z,0} H_\rho \Omega = F_{\rm max}. \tag{12}$$

Here we adopt the same α ansatz as in the standard thin disk model that the vertical integrated stress is related to the midplane pressure ${P_{z,0}}^2$ and density scale height

$$H_\rho \equiv \frac{1}{\Omega}\sqrt{\frac{P_{z,0}}{\rho_{z,0}}}, \tag{13}$$

where $\rho_{z,0}$ is the midplane density. From the diffusion equation

$$\frac{dP_r}{dz} = -\frac{\rho\kappa_t F_{rz,0}}{c}, \tag{14}$$

we can define the flux weighted optical depth $\bar{\tau}$ as

$$\bar{\tau} \equiv \frac{1}{F_{\rm max}}\int_0^{L_z/2} \rho\kappa_t F_{r,z0} dz. \tag{15}$$

Then the cooling rate per unit area $Q^- = F_{\rm max} = cP_{rz,0}/\bar{\tau}$ and $P_{rz,0} \approx P_{z,0}$ in the radiation pressure dominated regime. Because $F_{rz,0} = 0$ at the disk midplane where maximum density is located and $F_{\rm max}$ has contributions from both the diffusive and advective components, $\bar{\tau}$ is smaller than τ_0. Advection flux also changes

[2] Note that α defined this way is the ratio of the vertically integrated stress to the product of midplane pressure and the density scale, which can differ from the ratio of the vertically integrated stress to the vertically integrated pressure shown in Figure 1.

the vertical density profiles of the disk and it causes a stronger dependence of $\bar{\tau}$ on the midplane pressure compared with τ_0 as shown at the bottom panel of Figure 3 for OPALR20. To separate the effects of the opacity change with temperature and the advection flux, we calculate

$$\bar{\tau}_{\rm es} \equiv \frac{1}{F_{\rm max}} \int_0^{L_z/2} \rho \kappa_{\rm es} F_{r,z0} dz. \quad (16)$$

For the run OPALR20, $\bar{\tau} \propto P_{z,0}^{-2.90}, \tau_0 \propto P_{z,0}^{-0.89}$ while $\bar{\tau}_{\rm es} \propto P_{z,0}^{-2.10}$, which confirms that the change of $\bar{\tau}$ is the combined effect of τ_0 and $\bar{\tau}_{\rm es}$. For comparison, the bottom panel of Figure 6 shows that in the run ESR20c with electron scattering and free-free opacities, $\bar{\tau}$ only changes with midplane pressure as $P_{z,0}^{-0.17}$ while τ_0 is almost a constant as expected. Notice that the midplane gas pressure is already half of the radiation pressure at the end of this run and $Q \neq P_{z,0}/(c\bar{\tau})$.

Compared with the classical argument of thermal instability (Shakura & Sunyaev 1976; Piran 1978; Pringle 1981), $Q^- \propto P_{z,0}/\tau_0$. When electron scattering opacity dominates τ_0 is expected to be nearly constant because the surface density changes on timescale much longer than the thermal time scale. However, with iron opacity, we find that $Q^- \propto P_{z,0}/\bar{\tau}$ can increase much more sensitively with $P_{z,0}$ than the standard model predicts. Since the sensitivity of Q^+ to $P_{z,0}$ is not significantly affected by the additional iron opacity, Q^+ and Q^- can have rather similar dependencies on midplane pressure. This is consistent with thermal runaway being significantly slower and possibly absent in OPALR20, but occurring rapidly in the electron scattering dominated runs.

Since we cannot determine how the effects of iron opacity peak change with different accretion rates with the available simulations, we parametrize $\bar{\tau}$ as

$$\bar{\tau} \equiv \beta \frac{\kappa_{\rm es}\Sigma}{2}. \quad (17)$$

Therefore, the Σ, $P_{z,0}$ and H_ρ are related to $F_{\rm max}$ and Ω as

$$H_\rho = \frac{\beta\kappa_{\rm es}}{c}\frac{F_{\rm max}}{\Omega^2},$$
$$P_{z,0} = \frac{c}{\beta\kappa_{\rm es}\alpha}\Omega,$$
$$\Sigma = 2\rho_{z,0}H_\rho = \frac{2c^2}{\beta^2\kappa_{\rm es}^2\alpha}\frac{\Omega}{F_{\rm max}}. \quad (18)$$

To connect to the radial structures of the accretion disk, the radiation flux can be related to the accretion rate $\dot{M}$ as (Shakura & Sunyaev 1973; Frank et al. 2002)

$$F_{\rm max} = \frac{3GM_{\rm BH}\dot{M}}{8\pi r_0^3}. \quad (19)$$

If we scale the accretion rate with the Eddington accretion rate $\dot{M}_{\rm Edd} = 40\pi GM_{\rm BH}/(c\kappa_{\rm es})$ as $\dot{m} \equiv \dot{M}/\dot{M}_{\rm Edd}$, and scale the radius with the Schwarzschild radius $r_s = 2GM_{\rm BH}/c^2$ as $r \equiv r_0/r_s$, the equations can be simplified as

$$H_\rho = \frac{15}{2}\beta r_s \dot{m},$$
$$P_{z,0} = \frac{\sqrt{2}}{2}\frac{c^2}{\beta\kappa_{\rm es}\alpha r_s}\frac{1}{r^{3/2}},$$
$$\Sigma = \frac{4\sqrt{2}}{15}\frac{r^{3/2}}{\beta^2\alpha\kappa_{\rm es}\dot{m}}. \quad (20)$$

If we set $\beta = 1$, we recover the scaling relations in the radiation pressure dominated α disk model. This is also similar to the analysis done in the Appendix A of (Hirose et al. 2009a). The time averaged $\beta = 0.4$ for the run OPALR20. Calibrating β for different $\dot{m}$ and r will be the focus of our future work.

In the α disk model, there is a maximum surface density that can support a thermal equilibrium state in the so-called S-curve (Lightman & Eardley 1974; Hirose et al. 2009a) and the surface density in OPALR20 is *larger* than this maximum if $\beta = 1$. If we simply increase the opacity in the α disk model to account for the additional iron opacity, this maximum surface density would *decrease*. However, the effect of the enhanced advection on the flux weighted opacity $\bar{\tau}$ keeps $\beta < 1$, so that the maximum surface density can be consistent with the larger surface density in OPALR20.

5.2. *Implications for AGN Observations*

The bolometric luminosity of most AGNs are observed to be smaller than the Eddington luminosity defined using only the electron scattering opacity (Heckman et al. 2004; Kelly et al. 2010). Therefore, the accretion disks of most AGNs are thought to be adequately described by the standard thin disk model. No significant outflow driven by the continuum radiation is expected. However, when the opacity is enhanced significantly by bound-bound transition of Fe, the effective radiation acceleration can be comparable or even larger than the gravitational acceleration. In other words, the Eddington ratio defined by the electron scattering opacity is no longer relevant. Therefore, similar to the case of massive stars (Smith 2014), radiation acceleration via the iron opacity bump has the potential to drive significant outflow, even though the normal Eddington ratio is smaller than 1. Since the location of the iron opacity bump is relatively close to the central supermassive black hole (20 r_s for the simulation OPALR20) and it will move inward with increasing black hole mass, the velocity of any possible outflow driven from this region could be on the order of the Keplerian rotation velocity, which might be much faster than the outflow driven by the line opacity in previous models (Murray et al. 1995; Proga et al. 2000). This makes it a possible candidate for the launching of ultra-fast outflows (Tombesi et al. 2010, 2015). The spectral energy distributions of most AGNs usually show a turnover around 1000 Å as discussed in the Introduction, and Laor & Davis (2014) suggests that significant outflow driven by UV line opacity might explain this. The iron opacity bump may play a dominant role in the launching of such an outflow.

The enhancement of the opacity due to iron also depends on the metallicity. The iron opacity bump should increase with increasing metallicity (Paxton et al. 2011). The simulation OPALR20 assumes solar metallicity as an example, but the metallicity in AGNs can be supersolar (Hamann & Ferland 1993; Arav et al. 2007; Fields et al. 2007). Therefore, this simulation may underestimate the

role that the iron opacity bump plays in stabilizing the disk, modifying the vertical structure, and potentially driving an outflow. On the other hand, if the metallicity in some AGN disks is much smaller, the iron opacity bump will be weaker and thermal instability may still exist, although the growth time scale of the thermal instability may still be longer than the thermal time scale as predicted by the α disk model. This perhaps is one explanation for the recently discovered "change look" AGNs (LaMassa et al. 2015; Ruan et al. 2015; Runnoe et al. 2016) but the significant change of luminosity within a few years does not happen for other AGNs.

Due to the sensitive dependence of the iron opacity bump on the temperature, it will only play an important role in a certain radial range of the accretion disks in AGNs, since the midplane temperature of the disk decreases with increasing radius for a fixed accretion rate. The iron opacity bump only exists around 1.8×10^5 K. Therefore, it will be absent in hotter regions of the disk where the effective temperature is larger than this value, but may still be relevant near the midplane in regions of the disk where the effective temperature is much lower (e.g. $\sim 2 \times 10^4$ K in OPALR20). This suggests that the region where the iron opacity bump is most important is between the innermost region where extreme UV or soft X-rays would be emitted and regions further out where longer wavelength UV photons are emitted. Since the effective Eddington ratio in the region with the iron opacity bump is larger, the height of the photosphere in this region will likely larger than in hotter, neighboring regions closer to the black hole where electron scattering opacity would dominate. This could lead to a sharp drop in the scale height when radius decreases and provide a "bump" to shield the outer UV emitting disk from X-ray photons emitted in the inner region. Since the outer UV photons are thought to accelerate broad absorption line outflows through line driving (Proga et al. 2000), this geometry might help shield the outflows from over ionization by the X-rays (Higginbottom et al. 2014). Such a geometry may also explain some properties of weak line quasars (Luo et al. 2015). A sharp drop in the scale height as radius decreases would also provide a surface for intercepting X-ray photons emitted in the inner disk without the need for a large scale height for the X-ray emitting region. This may naturally explain the level of X-ray irradiation inferred from correlated variability of UV and X-rays bands (Edelson et al. 1996, 2015) and may even alter the radial distribution of the UV emission if the irradiating flux is large enough. Ultimately, global radiation MHD simulations will be needed to understand the effects of the iron opacity bump on the global structure of the disk to determine if these speculations are correct.

ACKNOWLEDGEMENTS

Y.F.J. thanks Omer Blaes, Jeremy Goodman, Daniel Proga and Eliot Quataert for helpful discussions. This work benefited from our participation in an International Space Science Institute meeting. This work was supported by the computational resources provided by the NASA High-End Computing (HEC) Program through the NASA Advanced Supercomputing (NAS) Division at Ames Research Center; the Extreme Science and Engineering Discovery Environment (XSEDE), which is supported by National Science Foundation grant number ACI-1053575; and the computer cluster Rivanna at the University of Virginia. Y.F.J. is supported by NASA through Einstein Postdoctoral Fellowship grant number PF3-140109 awarded by the Chandra X-ray Center, which is operated by the Smithsonian Astrophysical Observatory for NASA under contract NAS8-03060. S.W.D. is supported by a Sloan Foundation Research Fellowship. We acknowledge support from NSF grant AST-1333091 "Collaborative Research: Black Hole Accretion Theory and Computation Network".

REFERENCES

Arav, N., Gabel, J. R., Korista, K. T., et al. 2007, ApJ, 658, 829
Balbus, S. A., & Hawley, J. F. 1991, ApJ, 376, 214
Blackburne, J. A., Pooley, D., Rappaport, S., & Schechter, P. L. 2011, ApJ, 729, 34
Blaes, O., Krolik, J. H., Hirose, S., & Shabaltas, N. 2011, ApJ, 733, 110
Bonning, E. W., Cheng, L., Shields, G. A., Salviander, S., & Gebhardt, K. 2007, ApJ, 659, 211
Crummy, J., Fabian, A. C., Gallo, L., & Ross, R. R. 2006, MNRAS, 365, 1067
Davis, S. W., Stone, J. M., & Jiang, Y.-F. 2012, ApJS, 199, 9
Davis, S. W., Woo, J.-H., & Blaes, O. M. 2007, ApJ, 668, 682
Dhanda, N., Baldwin, J. A., Bentz, M. C., & Osmer, P. S. 2007, ApJ, 658, 804
Done, C. 2014, in Suzaku-MAXI 2014: Expanding the Frontiers of the X-ray Universe, ed. M. Ishida, R. Petre, & K. Mitsuda, 300
Done, C., Davis, S. W., Jin, C., Blaes, O., & Ward, M. 2012, MNRAS, 420, 1848
Edelson, R., Gelbord, J. M., Horne, K., et al. 2015, ApJ, 806, 129
Edelson, R. A., Alexander, T., Crenshaw, D. M., et al. 1996, ApJ, 470, 364
Elvis, M., Wilkes, B. J., McDowell, J. C., et al. 1994, ApJS, 95, 1
Fields, D. L., Mathur, S., Krongold, Y., Williams, R., & Nicastro, F. 2007, ApJ, 666, 828
Frank, J., King, A., & Raine, D. J. 2002, Accretion Power in Astrophysics: Third Edition (Cambridge University Press, Cambridge, UK)
Guan, X., Gammie, C. F., Simon, J. B., & Johnson, B. M. 2009, ApJ, 694, 1010
Hamann, F., & Ferland, G. 1993, ApJ, 418, 11
Hawley, J. F., Guan, X., & Krolik, J. H. 2011, ApJ, 738, 84
Heckman, T. M., Kauffmann, G., Brinchmann, J., et al. 2004, ApJ, 613, 109
Higginbottom, N., Proga, D., Knigge, C., et al. 2014, ApJ, 789, 19
Hirose, S., Blaes, O., & Krolik, J. H. 2009a, ApJ, 704, 781
Hirose, S., Blaes, O., Krolik, J. H., Coleman, M. S. B., & Sano, T. 2014, ApJ, 787, 1
Hirose, S., Krolik, J. H., & Blaes, O. 2009b, ApJ, 691, 16
Hirose, S., Krolik, J. H., & Stone, J. M. 2006, ApJ, 640, 901
Iglesias, C. A., & Rogers, F. J. 1996, ApJ, 464, 943
Jiang, Y.-F., Cantiello, M., Bildsten, L., Quataert, E., & Blaes, O. 2015, ApJ, 813, 74
Jiang, Y.-F., Stone, J. M., & Davis, S. W. 2012, ApJS, 199, 14
—. 2013a, ApJ, 778, 65
—. 2013b, ApJ, 767, 148
—. 2014a, ApJ, 796, 106
—. 2014b, ApJ, 784, 169
Kelly, B. C., Vestergaard, M., Fan, X., et al. 2010, ApJ, 719, 1315
Koratkar, A., & Blaes, O. 1999, PASP, 111, 1
LaMassa, S. M., Cales, S., Moran, E. C., et al. 2015, ApJ, 800, 144
Laor, A., & Davis, S. W. 2014, MNRAS, 438, 3024
Lasota, J.-P. 2001, New Astronomy Reviews, 45, 449
Lightman, A. P., & Eardley, D. M. 1974, ApJ, 187, L1
Luo, B., Brandt, W. N., Hall, P. B., et al. 2015, ApJ, 805, 122
Malkan, M. A. 1983, ApJ, 268, 582
Merloni, A. 2003, MNRAS, 341, 1051
Miller, K. A., & Stone, J. M. 2000, ApJ, 534, 398
Morgan, C. W., Kochanek, C. S., Morgan, N. D., & Falco, E. E. 2010, ApJ, 712, 1129

Murray, N., Chiang, J., Grossman, S. A., & Voit, G. M. 1995, ApJ, 451, 498
Paxton, B., Bildsten, L., Dotter, A., et al. 2011, ApJS, 192, 3
Piran, T. 1978, ApJ, 221, 652
Pringle, J. E. 1981, ARA&A, 19, 137
Proga, D., Stone, J. M., & Kallman, T. R. 2000, ApJ, 543, 686
Ruan, J. J., Anderson, S. F., Cales, S. L., et al. 2015, arXiv:1509.03634
Runnoe, J. C., Cales, S., Ruan, J. J., et al. 2016, MNRAS, 455, 1691
Shakura, N. I., & Sunyaev, R. A. 1973, A&A, 24, 337
—. 1976, MNRAS, 175, 613
Shull, J. M., Stevans, M., & Danforth, C. W. 2012, ApJ, 752, 162
Smith, N. 2014, ARA&A, 52, 487
Sorathia, K. A., Reynolds, C. S., Stone, J. M., & Beckwith, K. 2012, ApJ, 749, 189
Stella, L., & Rosner, R. 1984, ApJ, 277, 312
Stone, J. M., Gardiner, T. A., Teuben, P., Hawley, J. F., & Simon, J. B. 2008, ApJS, 178, 137
Tombesi, F., Cappi, M., Reeves, J. N., et al. 2010, A&A, 521, A57
Tombesi, F., Meléndez, M., Veilleux, S., et al. 2015, Nature, 519, 436
Turner, N. J. 2004, ApJ, 605, L45
Turner, N. J., Stone, J. M., Krolik, J. H., & Sano, T. 2003, ApJ, 593, 992
Zheng, W., Kriss, G. A., Telfer, R. C., Grimes, J. P., & Davidsen, A. F. 1997, ApJ, 475, 469